

# PLD Epitaxial Thin-Film BaTiO<sub>3</sub> on MgO – Dielectric and Electro-Optic Properties

## Journal Article

### Author(s):

Winiger, Joel; Keller, Killian; Moor, David ; Baumann, Michael ; Kim, Donghoon; Chelladurai, Daniel ; Kohli, Manuel; Blatter, Tobias; Dénervaud, Eric; Fedoryshyn, Yuriy; Koch, Ueli ; Pané, Salvador; Grange, Rachel ; Leuthold, Juerg 

### Publication date:

2024-01-04

### Permanent link:

<https://doi.org/https://doi.org/10.3929/ethz-b-000637314>

### Rights / license:

[Creative Commons Attribution 4.0 International](#)

### Originally published in:

Advanced Materials Interfaces 11(1), <https://doi.org/10.1002/admi.202300665>

### Funding acknowledgement:

- Neuro-augmented 112Gbaud CMOS plasmonic transceiver platform for Intra- and Inter-DCI ()
- Energy- and Size-efficient Ultra-fast Plasmonic Circuits for Neuromorphic Computing Architectures ()
- Nonlinear Pockels Materials for Nanoscale Devices ()

# PLD Epitaxial Thin-Film BaTiO<sub>3</sub> on MgO – Dielectric and Electro-Optic Properties

Joel Winiger,\* Killian Keller, David Moor, Michael Baumann, Donghoon Kim, Daniel Chelladurai, Manuel Kohli, Tobias Blatter, Eric Dénervaud, Yuriy Fedoryshyn, Ueli Koch, Salvador Pané, Rachel Grange, and Juerg Leuthold

The study demonstrates high-quality pulsed-laser-deposited (PLD) barium titanate (BTO) thin-films on a magnesium oxide substrate. The frequency response of the relative permittivity (dielectric constant) and the linear electro-optical coefficient (Pockels coefficient) are measured. At 0.2 GHz, the Pockels coefficient is fitted to be  $r_{42} \approx 1030 \text{ pm V}^{-1}$ . It decreases to  $\approx 390 \text{ pm V}^{-1}$  at 10 GHz after which it remains constant up to 70 GHz. The unbiased BTO permittivity is measured to be  $\epsilon_a \approx 7600$  at 0.2 GHz, dropping to  $\approx 1100$  at 67 GHz, while the biased BTO had a permittivity  $\epsilon_a \approx 2000$  at 0.2 GHz, dropping to  $\approx 500$  at 67 GHz. These results fill an important experimental characterization gap for high-speed BTO applications and show the high quality of PLD-grown BTO films. Lastly, the material's crystalline quality is characterized and the domain distribution is imaged. The findings enable the design and fabrication of a new generation of BTO-based components for sensing and communications.

## 1. Introduction

BTO showcases one of the largest known Pockels coefficients, making it an ideal candidate for footprint reduction of next-generation high-bandwidth modulators in photonic integrated circuits (PICs) for Tbit/s links.<sup>[1]</sup> Toward this goal, different electro-optic effects are utilized such as the plasma dispersion effect, the quantum-confined Stark effect, and the linear electro-optic (Pockels) effect.<sup>[2]</sup> Among these effects, the Pockels effect is of particular interest due to its ultra-fast and linear response, as well as its capability to provide pure phase modulation. Therefore, the growth, characterization, and integration of high-quality linear electro-optic materials have gained paramount importance.

Presently, the prevailing solid-state Pockels material employed in modulators is lithium niobate (LiNbO<sub>3</sub>, LNB), exhibiting a Pockels coefficient  $r_{33} = 31 \text{ pm V}^{-1}$  at GHz modulating frequencies.<sup>[3]</sup> Yet, the limited electro-optic coefficient results in millimeter-long modulators, making the design of high-speed modulators challenging.<sup>[4]</sup> A possibility to reduce the interaction length and improve the bandwidth is by using electro-optic materials with higher Pockels coefficients. This has led to intense research in barium titanate (BTO).

Fabrication of thin-film BTO has been shown by a variety of methods. For instance, BTO has been grown using metal-organic chemical vapor deposition (MOCVD) or sol-gel deposition.<sup>[5]</sup> Yet, these techniques lead to polycrystalline films with reduced effective Pockels coefficient. BTO of higher quality can be obtained by molecular-beam epitaxy (MBE), pulsed laser deposition (PLD), or sputtering. These three methods provide BTO with aligned crystalline domains. While MBE permits to deposit of BTO on a large scale and precise control, it not only requires extensive expertise but also expensive tools. Conversely, PLD and sputtering are simpler, cheaper, and more commonly available growth techniques.

Meanwhile, there are multiple ways to fabricate BTO but only little data regarding the relative permittivity and the linear electro-optic effect of thin film BTO at radio frequencies (RF). At low speeds (< 10 MHz), piezo-electric effects cause the unit cell

J. Winiger, K. Keller, D. Moor, M. Baumann, D. Chelladurai, M. Kohli, T. Blatter, Y. Fedoryshyn, U. Koch, J. Leuthold  
 ETH Zurich  
 D-ITET


Institute of Electromagnetic Fields  
 Gloriastrasse 35, Zurich 8092, Switzerland  
 E-mail: winigerj@ethz.ch

D. Kim, S. Pané  
 ETH Zurich  
 D-MAVT

Institute of Robotics and Intelligent Systems  
 Tannenstrasse 3, Zurich 8092, Switzerland

E. Dénervaud, R. Grange  
 ETH Zurich  
 D-PHYS

Institute for Quantum Electronics  
 Optical Nanomaterial Group  
 Auguste-Piccard-Hof 1, Zurich 8093, Switzerland

 The ORCID identification number(s) for the author(s) of this article can be found under <https://doi.org/10.1002/admi.202300665>

© 2023 The Authors. Advanced Materials Interfaces published by Wiley-VCH GmbH. This is an open access article under the terms of the Creative Commons Attribution License, which permits use, distribution and reproduction in any medium, provided the original work is properly cited.

DOI: 10.1002/admi.202300665

to deform with an applied electric field. This mechanism significantly contributes to its polarizability and is defined as the stress-free or unclamped state of BTO. In literature, unclamped permittivities of room temperature bulk BTO in unbiased single crystal specimen  $\epsilon_{11} \approx 4400$  and  $6000$  are reported.<sup>[6]</sup> As can be seen, the values are quite different depending on the source. The unclamped Pockels coefficient for bulk BTO is reported to be  $r_{51} = r_{42} \approx 1300 \text{ pm V}^{-1}$  at  $630 \text{ nm}$  wavelength and  $r_{42} \approx 1000 \text{ pm V}^{-1}$  at  $1550 \text{ nm}$ .<sup>[6a,7]</sup> As the frequency increases from MHz to several GHz, crystal deformations cannot follow the electric field anymore. Therefore, only the strong and complex ionic  $\text{Ti}^{4+}$  movements along the *c*-axis [001] and the *a*-axes [100] and [010] remain significant contributors. The permittivities at these higher frequencies drop to  $\epsilon_{11} = \epsilon_a \approx 2180$  and  $\approx 500$  in clamped bulk BTO.<sup>[6]</sup> Likewise in the clamped case, the Pockels coefficients drop to  $\approx 730 \text{ pm V}^{-1}$  (at  $630 \text{ nm}$ ) and  $\approx 550 \text{ pm V}^{-1}$  (at  $1550 \text{ nm}$ ).<sup>[6a,7]</sup> Both, the relative permittivity and the Pockels coefficients, relax significantly when transitioning from the clamped to the unclamped regime, after which the electro-optic response remains constant up to up to  $300 \text{ GHz}$ .<sup>[8]</sup> Above  $300 \text{ GHz}$ , Raman measurements indicate a further reduction of the permittivity to  $\approx 60$  for single domain BTO crystals.<sup>[9]</sup> At even higher frequencies  $\approx 5 \text{ THz}$ , the permittivity slightly drops further until only a rather small electron polarizability will contribute.<sup>[10]</sup> In summary, while there is quite some work on the dielectric properties of BTO below and above the GHz frequency range, there is little data on the frequency response of the permittivity and none on the linear electro-optic coefficients of BTO across the important spectral range from  $100 \text{ s}$  of MHz up to  $10 \text{ s}$  of GHz.<sup>[6b,9–11]</sup> Additionally, much of the information as cited above, stems from bulk rather than thin-film BTO. Yet, it is thin-film BTO that currently is used for integrated optical applications. Lastly, it is unclear if the quality of BTO fabricated by PLD can provide as good dielectric and electro-optic properties as MBE-grown BTO. In some initial publications, various BTO deposition techniques were compared on the resulting electro-optic strength and found indications that MBE-grown BTO is superior in its electro-optic response.<sup>[12]</sup>

In this work, we show experimentally measured values of both the permittivity and the  $r_{42}$  Pockels coefficient of PLD-grown BTO on MgO substrate. The measurements cover the frequency range from  $200 \text{ MHz}$  up to  $70 \text{ GHz}$ . We find that the PLD-grown BTO is of high quality and that the values agree well with bulk BTO values (where accessible). The measurements thus not only close the frequency gap in literature but also answer a debate showing that PLD-grown BTO may be as good as bulk BTO or BTO fabricated by other techniques.<sup>[12b]</sup> Furthermore, we analyzed the crystalline microstructure of the PLD-grown BTO thin-film on MgO. We investigated the film's crystallinity with X-ray diffraction, and its growth quality with transmission electron microscopy and mapped the domain orientations through second-harmonic generation measurements. All of the findings are key in terms of understanding and designing future electro-optic devices with BTO.

## 2. Plasmonic Device for Characterization

Accurately measuring the permittivity and linear electro-optic (EO) coefficient at RF poses particular challenges. When the electrical wavelength shrinks to the scale of the photonic device un-

der test (DUT), the walk-off effects of optical and RF fields need to be considered. To avoid the complexity arising from the utilization of traveling wave electrodes, a viable approach is to leverage the significant enhancement offered by plasmonic devices, drastically reducing the device length and allowing the measurements to remain within the lumped-element regime. This section outlines the fabricated device designed to measure the dielectric and Pockels coefficients.

**Figure 1a–c** shows the top view of a plasmonic phase shifter with its cross-sections. The plasmonic section is formed by two gold pads placed on both sides of the BTO ridge, c.f. **Figure 1c**, serving as both electrodes and plasmonic waveguide. The device operates as follows. A TE-polarized continuous-wave laser at  $1550 \text{ nm}$  is fed through a silicon access waveguide, see **Figure 1b**, into the plasmonic slot waveguide, see **Figure 1c**. Upon applying an electrical field across the plasmonic slot, the optical signal is modulated by means of the linear electro-optic effect in BTO. The coupling of the laser in and out of the chip is achieved through silicon grating couplers.

The plasmonic section provides a high confinement and a good overlap between the optical and RF fields, leading to a significant enhancement of the light–matter interaction. As a result, the length of the plasmonic section can be kept as short as  $10 \mu\text{m}$ , which is well below the RF wavelength and effectively making it an electrically lumped element. This simplifies the analysis by eliminating considerations of characteristic impedance and phase matching.

BTO is known to grow either in-plane or out-of-plane. When BTO is grown on substrates with a slightly larger lattice constant above  $700 \text{ }^\circ\text{C}$ , usually its layer stack initially comprises in-plane BTO.<sup>[13]</sup> Here, its *c*-axis crystalline structure lies in-plane and tends to grow in domains that are aligned by  $0^\circ$  and  $90^\circ$  against the crystalline structure of the substrate, see **Figure 1d,e**. To fully exploit the largest Pockels coefficient  $r_{42} = r_{zy} = r_{zx}$  in such perpendicularly oriented domains, one orients the waveguide at a  $45^\circ$  angle with respect to the in-plane axis. This results in an effective Pockels coefficient  $r_{\text{eff}} = \sqrt{1/2} r_{42}$  as described in more detail in reference.<sup>[14]</sup> Once the layer stack reaches a thickness of  $\approx 40 \text{ nm}$ , its crystalline structure aligns vertically – or out-of-plane. The change of the *c*-axis with increasing thickness is depicted by the black arrows in **Figure 1b,c**.

## 3. Dielectric and Electro-Optic Results

This section presents the relative permittivity  $\epsilon_a$  and the Pockels coefficient  $r_{42}$  obtained from the plasmonic device measurements. They show the relaxation of BTO's polarizability with increasing frequency and the associated reduction in permittivity and Pockels coefficient. Further details on the analysis will be given in Section 5.

### 3.1. Relative Permittivity

The relative permittivity  $\epsilon_a$  of BTO in the frequency range from  $100 \text{ MHz}$  up to  $67 \text{ GHz}$  is plotted in **Figure 2** for a range of bias voltages, and two Debye relaxations were fitted to the data (see Experimental Section 7). The description through two Debye

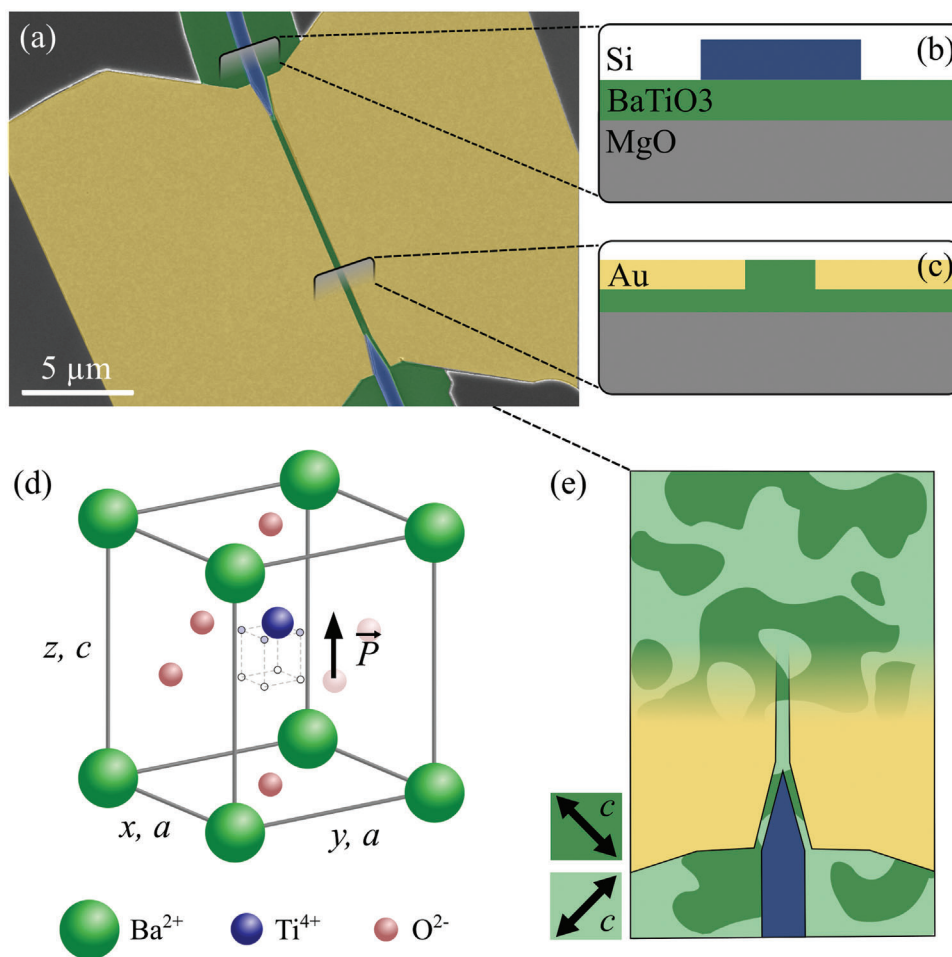


**Figure 1.** a) Colorized SEM image showing the plasmonic phase shifter. Signals are launched into the device through access waveguides in Si (colored in blue). The laser light is then fed into metal-BTO-metal slot waveguides. The gold metals are shown in yellow. The BTO electro-optic material is plotted in green. Cross-sections of the b) access- and c) slot waveguide regions, respectively. The orientation of the c-axis BTO in the respective layer stacks is indicated by a black arrow. d) BTO's unit cell in its tetragonal ferroelectric phase. The eight possible sites of the  $\text{Ti}^{4+}$  ion and its resulting remnant polarization are indicated in gray. e) A top-view illustration of in-plane BTO. Here, the device is oriented in a  $45^\circ$  angle with respect to the two domains of c-axis BTO's.

relaxations was suggested in 1994.<sup>[11c]</sup> The plot shows that the permittivity depends on the applied electric field. Similar findings have been reported for BTO by other authors.<sup>[6b,11f]</sup> In its pristine, unbiased state, we found a relative permittivity  $\epsilon_a \approx 7600$  at 0.2 GHz and thereafter a decrease to  $\approx 1100$  at 67 GHz. When gradually biasing the pristine BTO up to 5 V, we find that the permittivity drops to  $\epsilon_a \approx 2000$  at 0.2 GHz and  $\approx 500$  at 67 GHz.

To better visualize the permittivity's dependence on the applied bias voltage such as found in Figure 2, we extracted the permittivity at certain frequencies and plotted them against the electric field strength within BTO, as shown in Figure 3. It should be noted that the applied voltages and the field strengths within BTO must be derived from the true geometry in Figure 8 (see below). From this figure, it can be seen that the voltage in part drops off within silicon and across BTO. The real field in BTO can then be derived from simulations as the permittivity in silicon is well known.<sup>[15]</sup>

Figure 3 shows a large bias dependence at MHz frequencies, whereas only a small one above 10 GHz. This indicates that the bias influences the unclamped state.

The relative permittivity of BTO at RF as shown in Figures 2 and 3 was found by measuring the  $S_{11}$  parameter of our devices using a vector network analyzer. Note that the measured data is noisier toward low frequencies, as the impedance of the device approaches infinity due to the large capacitance. Further, we had a spurious 130 MHz sinusoidal signal, that was filtered using Fourier magnitude filtering, preserving the phase information. The lumped element nature of the plasmonic device allows us to approximate our device as an electrical circuit consisting of two parallel capacitances: the pad capacitance and the slot capacitance without any inductances. As a consequence, the imaginary part of the impedance stems from a pure capacitance. We can then isolate the contribution of the BTO slot and eliminate the constant capacitance from the pads by sweeping the length of the device. The contribution of the capacitance that changes its value

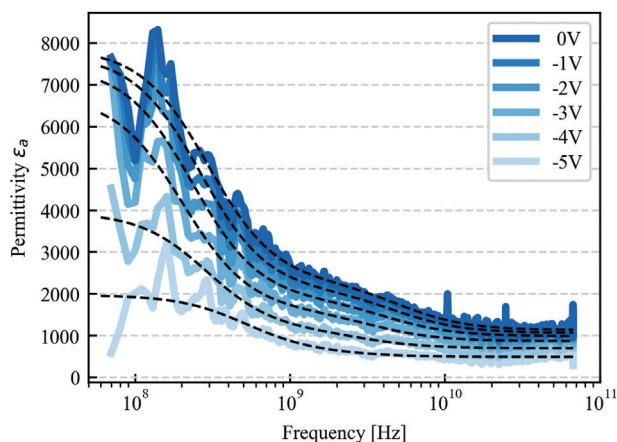


**Figure 2.** Measured permittivity  $\epsilon_a$  of BTO in the frequency range from 60 MHz to 70 GHz (solid lines). The dashed line is a fit with two Debye relaxators, see Experimental Section 7. The different shades correspond to a varying bias of 0 up to 5 V during the measurement and show BTO's permittivity dependence on a constant applied electric field.

must stem from the BTO, while the constant part accounts for the capacitance of the pads.

Once the capacitance of BTO for a certain frequency at a given bias field is known, the permittivity can be derived. Toward this goal, one needs the exact cross-section as further described in Section 4. One also needs to determine the ratio of in-plane versus out-of-plane BTO within the layer stack. This can be determined by XRD measurements (see Section 4). The in-plane BTO is dominated by the strong a-axis permittivity  $\epsilon_a$ . The c-axis contribution is weak ( $\epsilon_c/\epsilon_a < 3\%$ ) and therefore neglected.<sup>[11f]</sup> As our device is aligned by  $45^\circ$  with respect to the a-axis BTO domains, we account  $\epsilon_a$ 's contribution with a factor  $1/\sqrt{2}$ . Furthermore, as the in-plane oriented BTO has an a-axis and a c-axis aligned with the electric field,  $\epsilon_a$  is only contributing with a factor of  $1/\sqrt{2}$  to its effective permittivity. In the layer with the out-of-plane orientation BTO, two a-axis permittivities  $\epsilon_a$  contribute each with a weight of  $1/\sqrt{2}$ . These factors together with the replication of the

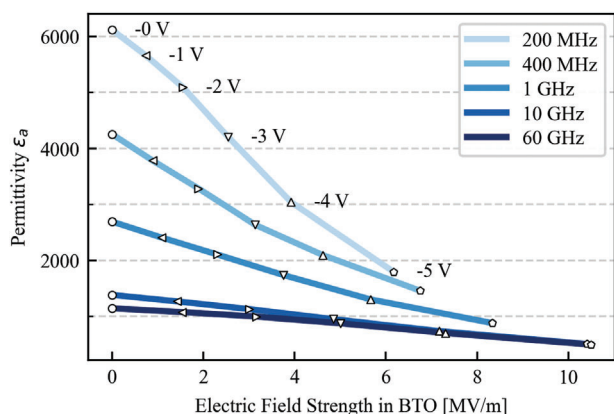


**Figure 3.** Measured permittivities from Figure 2 as a function of frequency plotted against the averaged electric field strength within BTO. A strong bias dependence is observed particularly at frequencies below 10 GHz. Same markers correspond to same applied bias voltage.

exact cross section are implemented into the capacitance simulation model. Within the simulation, BTO's permittivity is fitted such that the simulated capacitance matches the measured capacitance.

### 3.2. Pockels Coefficient

The frequency response of the Pockels coefficient of PLD-grown BTO is plotted in Figure 4 in the range from 200 MHz to 70 GHz. Because the Pockels coefficient is linked to the permittivity, the data can again be fitted with two Debye relaxators (see Experimental Section 7). Its unclamped value is  $1030 \text{ pm V}^{-1}$  at 0.2 GHz and decreases to  $390 \text{ pm V}^{-1}$  at 10 GHz. The standard deviations  $\pm 2\sigma$  against the mean are plotted in grey. The drop is usually associated with the piezoelectric and dipole-type relaxations as described in ref. [16]. The precise origin of the observed relaxation mechanism in BTO is challenging to determine, as it does not solely correspond to an order-disorder or a displacement mechanism.<sup>[16,17]</sup> For the measurements, we included results from six different devices with different slot widths ranging from 100 to 300 nm and lengths of 2, 5, and 10  $\mu\text{m}$ . The results do not show any trend that would relate to either length or width. This shows that the results do not suffer from any interface effects and represent the thin-film bulk coefficients.

To experimentally determine the values of BTO's EO strength in Figure 4, we used a tunable laser source to generate the optical carrier at 1550 nm, which is fed into the plasmonic slot. An electrical RF source with a slightly higher maximum output frequency than before was applied across the pads producing modulation sidebands via sum and difference frequency generation (SFG, DFG). These sidebands were measured using two different optical spectrum analyzers (OSA). A high resolution (5 MHz) OSA up to 15 GHz and a high dynamic range OSA for higher frequencies. From the magnitude of the sidebands, we derived the voltage-length product  $V_\pi L$ . The measured values were then compared with simulations that take into account the cross-section of the device, the orientation of BTO, the measured permittivity, and the measured refractive index at optical frequencies (2.27 at 1550 nm), as further elaborated in Section 4. The refractive index was obtained with a variable angle spectroscopic ellipsometer. By fitting the simulation to the measured results, we then determined the effective Pockels coefficient  $r_{\text{eff}}$ .<sup>[18]</sup>

To properly calculate the  $r_{\text{eff}}$  Pockels coefficient, one has to consider that the out-of-plane orientation's EO contribution is minimal, as the domains cannot be aligned and therefore cancel each other on average.

To derive  $r_{42}$  from  $r_{\text{eff}}$ , one needs to account for the tensorial nature of all second-order nonlinearities that contribute to the effective Pockels coefficient of BTO. For a plasmonic phase shifter at  $45^\circ$ , it is described in ref. [14]:

$$r_{\text{eff}} = \frac{1}{2\sqrt{2}} (r_{13} + r_{33} + 2r_{42}) \quad (1)$$

Based on literature values provided in ref. [6a], it becomes apparent that  $r_{33} = r_{zzz}$  is about a factor 30 weaker than  $r_{42} = r_{yzy}$ , and that  $r_{13} = r_{zxx}$  is even smaller. Thus, the two coefficients  $r_{13}$  and  $r_{33}$  can be considered negligible and  $r_{13}$  and  $r_{33}$  one can derive the Pockels coefficient  $r_{42}$  shown in Figure 4 from Equation (1).

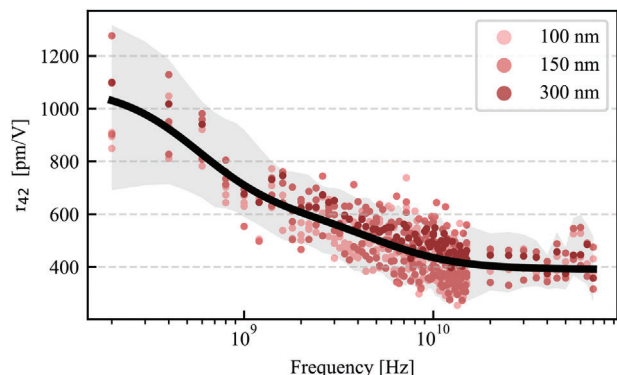


**Figure 4.** Pockels coefficient versus frequency in the range from 0.2 to 70 GHz. The red dots of different shade represent results derived from devices of different plasmonic slot widths (dark to bright: 300, 150, 100 nm). The black line is a fit with two Debye relaxators (see appendix), and the shaded area represents the standard deviation  $\pm 2\sigma$  from the mean value.

## 4. BTO Thin Film Characterization

To assess the importance of BTO's microstructure, it is crucial to understand the underlying processes that govern BTO's permittivity and electro-optic response. The ionic polarizability of BTO arises from a combination of both displacement and order-disorder polarization mechanisms.<sup>[6b,11c,17,19]</sup> On the one hand, the displacement mechanism accounts for the polarizability of BTO by considering charge separation due to the displacement of  $\text{Ti}^{4+}$  ions relative to their original site within the unit cell. On the other hand, the order-disorder model assumes that the  $\text{Ti}^{4+}$  occupies one of the eight corners of a hexahedron at the center of the unit cell, as depicted in Figure 1e. This tetragonality leads to a preference for the  $\text{Ti}^{4+}$  ions to occupy mostly the upper or lower four sites, resulting in a remnant polarization along the c-axis. The  $\text{Ti}^{4+}$  ions can freely move around to any of these four sites. As a consequence, the  $\text{Ti}^{4+}$  ions now may be displaced toward either side of the unit cell (i.e., within the a-plane). Therefore, the polarizability perpendicular to the c-axis exhibits a large permittivity. Simultaneously, the same strong non-centrosymmetric polarizability along the a-axis leads to a similar large electro-optic response.<sup>[16,20]</sup> This picture captures the particularly strong anisotropy in BTO and the large  $\epsilon_a$  and  $r_{42}$ . Further, it was shown that the strength and dynamic response cannot solely be explained by independent polarizations of single unit cells but require clusters on the order of  $8 \text{ nm}^3$  or 130  $\text{Ti}^{4+}$  ions that react simultaneously.<sup>[6b]</sup> This indicates that BTO's ferroelectric characteristics may not be found in nanometer-scale clusters.<sup>[21]</sup> Furthermore, other materials in the vicinity can influence BTO's behavior strongly, as they might screen its polarization.<sup>[21]</sup>

All insights above show that the epitaxial and crystalline state of the thin-films must be known and taken into account in order to assign the proper material constants. We, therefore, add here a section to determine the crystalline structure of the PLD-deposited BTO thin-film as used in these experiments.

### 4.1. Lattice Analysis

We analyzed the thin film with X-ray diffraction (XRD) by an out-of-plane  $\theta$ - $2\theta$  (parallel beam) scan. The measured spectrum was

fitted with two Voigt distributions as shown in Figure 5. The fit yielded lattice constants along the short a-axis of 4.00 Å and the longitudinal c-axis of 4.02 Å. These lattice parameters obtained from the fit are slightly larger than typical values reported in the literature (a-axis: 3.999 Å, c-axis: 4.0180 Å).<sup>[22]</sup> The literature values have been indicated by the vertical dashed line in the figure. Since we could not observe any other formation of other BTO orientations, the respective phase volume fraction of the a- and c-axis BTO can now be derived from the integrated intensity.<sup>[23]</sup> For this, we considered that a- and c-axis share the same crystal structural parameters and therefore the same structure factor but differ in the twofold multiplicity of the a-axis. We found that  $\approx 55\%$  of the thin-film exhibited an in-plane orientation, equivalent to a thickness of 50 nm, while the remaining  $\approx 45\%$  had an out-of-plane orientation, corresponding to a thickness of 40 nm. As further discussed in Section 5, we assume the initial layer growth is in-plane and becomes out-of-plane after 50 nm, as indicated in Figure 1b,c.

### 4.2. Domain Orientation

The size and orientation of the c-axis domains within an inplane BTO thin-film can be complex but is an important consideration for device simulations.<sup>[24]</sup> Its size distribution will also be the defining factor for any optical domain scattering losses.

A top-view plot with the in-plane polarization-resolved domain orientations is shown in Figure 6. The plots were obtained by a SHG microscope as discussed in the paragraph below. In contrast to single crystalline substrates, where domain sizes can span multiple micrometers, we found domain sizes in the order of one micrometer or below.<sup>[25]</sup> Further, one finds mainly two dominant crystal orientations as indicated by the identical colors. Opposite orientations are indistinguishable. Knowledge about the orientations plays a crucial role in maximizing the EO properties of BTO films, as multiple domains with different orientations either donot contribute (being orthogonal) or cancel (being aligned opposite) their effects. The plot thus shows that the realization of a single-domain device is not possible even within the small footprint of a plasmonic phase shifter. As most photonics devices will therefore extend over multiple domains, poling will be needed to

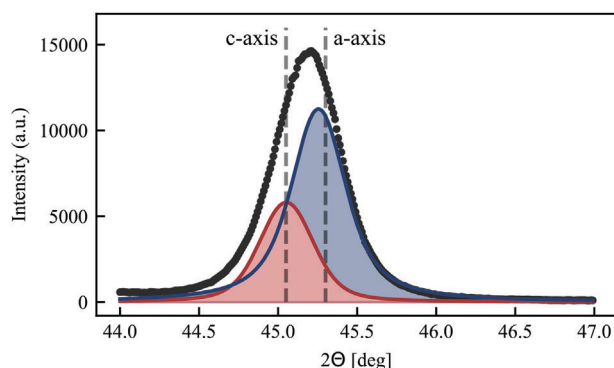


**Figure 5.** The  $\theta$ - $2\theta$  out-of-plane XRD measurement of the 90 nm BTO film. Dashed lines indicate literature values. The two Voigt fits show the proportion of in-plane (blue) and out-of-plane (red) orientation.

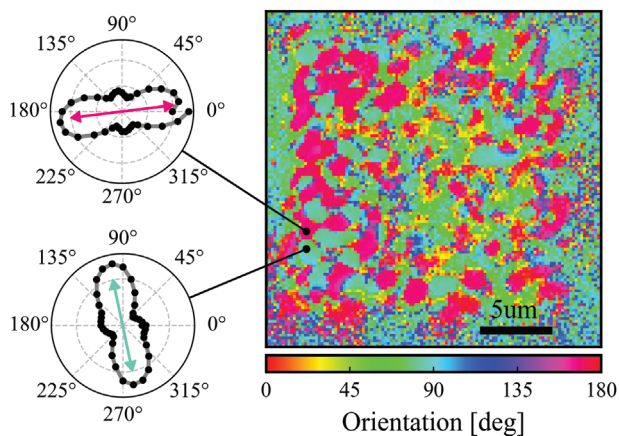


**Figure 6.** SHG reflection microscope image taken with at 20x objective. The polar plots give an example of the angle-resolved intensity measurement recorded at each pixel. The image is colored according to the dominant angle, as indicated in the polar plots.

make sure that domains with opposite orientations are aligned in the equal direction.

To find the domain distribution as shown in Figure 6, we analyzed the polarization dependence of second harmonic generation (SHG) in BTO by a fully-automated homemade nonlinear microscope system described elsewhere.<sup>[25,26]</sup> The experimental setup involved focusing a polarized tunable Ti:Sapphire laser onto the thin-film, while imaging the emitted SHG signal using a 20x objective. By rotating the polarizer, a series of images was acquired, and subsequently overlapped to create a composite image of the illuminated spot. To obtain a more comprehensive view, a larger area was scanned with overlapping measurement points, resulting in the domain distribution image shown in Figure 6. In this analysis, each pixel was colorized based on the dominant SHG signal angle, as indicated in the polar subplots. This technique allowed us to visualize the two perpendicular domain orientations of BTO corresponding to the (100) and (010) axes, with only little mixed areas having deviating angles. These intermediate angles are due to the finite optical resolution, as these pixels receive SHG signal from perpendicular domain boundaries.

#### 4.3. Hysteresis

To ensure the effective utilization of BTO's Pockels effect, it is crucial to align the domains in the material. Without domain alignment, the nonlinear optical effects of the domains would cancel each other on average, resulting in a diminished effective Pockels effect in an unpoled device. When applying a bias, the domains align and when fully oriented reach the bulk value as shown in Figure 7. This behavior is consistent with observations made in other BTO thin-films.<sup>[14]</sup> Upon removing the electric field, a remnant net polarization remains, characteristic of the hysteresis behavior exhibited by BTO.

To accurately measure the  $r_{42}$  Pockels value, it is necessary to operate the device with a bias voltage. Figure 6 illustrates the hysteresis measurement of two devices (300 nm and 100 nm slot width), where the initial polarization of the pristine device is indicated by the light red curve, and the subsequent voltage sweep

is represented by the dark red curve. It should be noted that some devices exhibit asymmetric behavior, while most others demonstrate the expected symmetric response. We cannot explain this asymmetry but assume it to be connected to domain screening and pinning, because there usually is no remnant polarization observed for the lower side of the sweep, as can be seen for device 2 in Figure 7 with a negative bias. Therefore, we measured the coercive field to always be close to zero, while the symmetric cases exhibit  $E_C \approx 10 \text{ kV mm}^{-1}$ .<sup>[27]</sup>

The required electric field strength for maximal alignment of the domains, thus maximal use of BTO's Pockels effect depends on the specific device geometry parameters, such as electrode distance and potential intermediate materials (i.e., Si). Even more, processes like aging and fatigue can reduce the necessary field strength and effective Pockels constant via unwanted accumulation of oxygen vacancies at domain boundaries, which screen them from reorientation.<sup>[28]</sup>

## 5. Discussion of Device Geometry & Simulation

For the determination of the permittivity and linear electro-optic constants, we require both the material characterizations described earlier and the precise cross-section of the device. In this section, we elaborate on these important details and how they were replicated in simulation. Note that the data presented above did already take these findings into account.

### 5.1. Cross-Section

A detailed cross-section of the device as shown in Figure 8a was captured by extracting and analyzing a  $\approx 50 \text{ nm}$  thin lamella of the plasmonic section from one of the measured devices. Focused ion beam milling (TFS Helios 5ux) and high-resolution imaging techniques (Talos F200x G2) were employed to prepare and examine the specimen. The high angular annular dark field (HAADF) signal provided strong material contrast in the

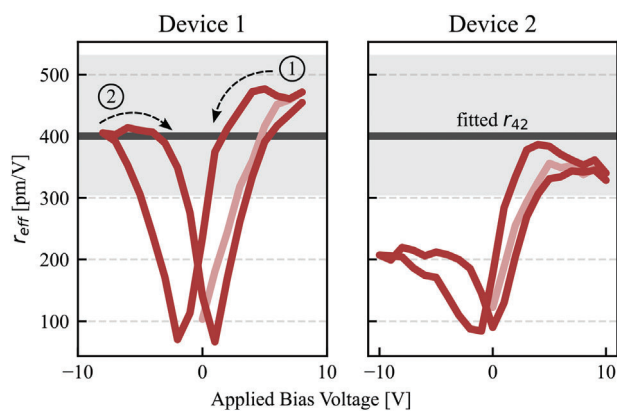


**Figure 7.** The effective  $r_{42}$  hysteresis occurring from domain alignments as found when sweeping the bias voltage during sideband measurements at 25 GHz. Most devices feature a symmetric (device 1) curve. Some devices exhibited an asymmetric (device 2) behavior. The averaged  $r_{42}$  line and its shaded background corresponds to the measurements from Figure 4 at 25 GHz.

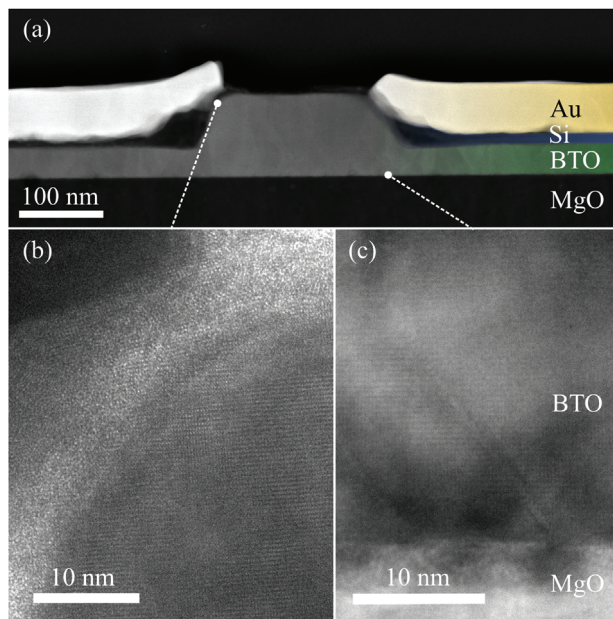


**Figure 8.** a) HAADF image of the cross section. b,c) HRTEM images showing the crystalline state of BTO up to its interface with the residual polycrystalline Si layer.

cross-section, enabling clear differentiation between materials. To determine the exact atomic species, position-dependent energy-dispersive X-ray spectroscopy was performed. The analysis confirmed the presence of the intended materials and revealed no indication of additional formations such as  $\text{SiO}_2$  or  $\text{TiO}_2$ . Further, it shows a residual few-nanometer-thick Si layers.

High-resolution transmission electron microscopy (HRTEM) was utilized to investigate the atomic structure of the layers. Figure 8b depicts a HRTEM image, showing that all present materials exhibit a (poly-)crystalline state, including the interfaces. Another HRTEM image at the BTO/MgO boundary shows lattice-mismatch-induced defects that form within the first few tens of nanometers of the film. This observation, in conjunction with the XRD measurement and the fact that BTO was grown on MgO at high temperature, suggests that BTO initially grows in a stressed in-plane fashion, similar to the findings in ref. [13]. The accumulated strain is subsequently relieved through the formation of defects. Eventually, the growth turns into an out-of-plane orientation. A thorough analysis of polarization transitions of BTO is given in ref. [29].

## 5.2. Simulation Considerations

To analyze and derive results from our dielectric and optical measurements, finite element simulations of RF and optical fields were performed using COMSOL. The exact cross-section described in the previous section was recreated in the simulation model (Figure 9) and considers the crystalline intermediate silicon layer, as well as BTO's domain orientations (as explained above). To determine BTO's relative permittivity, we adjusted it within the simulation such that it fitted the measured capacitance. An example voltage distribution for  $\epsilon_{\text{BTO},a} = 1000$  is shown in Figure 9a.

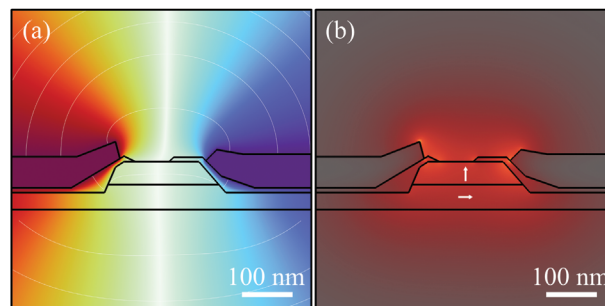


**Figure 9.** a) The simulated voltage drop of the RF signal across the slot and b) the magnitude-squared of the electric field at optical frequency. The arrows in (b) indicate the assumed domain orientation of BTO within the film.

Additional considerations are needed to conclude on BTO's electro-optic strength. The measured SFG efficiency, which corresponds to the effective Pockels coefficient, depends on the weighted overlap of the optical mode with the electrical RF field within BTO. Further, the simulation includes the measured in- and out-of-plane orientation of the film, the measured dielectric constant of BTO, and the measured refractive index at 1550 nm ( $n = 2.27$ ). The normalized electric field mode profile of such a simulation is shown in Figure 9b. Finally, the simulation is run with and without an applied electric field and the resulting two mode indices are extracted. The index difference then relates to the strength of BTO's Pockels coefficient and defines the device's  $V_\pi$  through:

$$V_\pi = \frac{\lambda_0}{2L} \left( \frac{\Delta V}{\Delta n} \right) \quad (2)$$

with  $\Delta V$  as the applied voltage,  $\Delta n$  the simulated change in the effective index of the plasmonic mode,  $\lambda_0$  the optical wavelength and  $L$  the device length. By fitting the simulated  $V_\pi$  to the measured  $V_\pi$  obtained from the sideband measurements (as explained in ref. [18]), the effective Pockels coefficient was derived. This value was then used in Equation (1) to conclude on the measured  $r_{42}$ , as shown in Figure 4.

## 6. Conclusion

In this work, we determined the a-axis permittivity and electro-optic response of PLD-grown thin-film BTO on a MgO substrate. We find an unbiased permittivity of  $\epsilon_a \approx 6700$  at 0.2 GHz and 1100 at 67 GHz. In the biased case, these values drop to  $\epsilon_a \approx 2000$  at 0.2 GHz and 500 at 67 GHz. We then highlighted the measured bulk-like electro-optic response of  $r_{42} = 1030 \text{ pm V}^{-1}$  at <0.2 GHz and its subsequent drop to a value of  $390 \text{ pm V}^{-1}$  above 10 GHz and up to 70 GHz. This result fills a significant frequency gap in

**Table 1.** Obtained parameters for fitting  $r_{42}$  with Equation (3).

$S_R$	$\gamma_R$ [MHz]	$S_r$	$\gamma_r$ [GHz]	$\epsilon_\infty$
487	574	206	5.15	391

**Table 2.** Obtained parameters for fitting  $\epsilon_a$  with Equation (3).

Bias [V]	$S_R$	$\gamma_R$ [MHz]	$S_r$	$\gamma_r$ [GHz]	$\epsilon_\infty$
0	5585	296	1149	5.18	1134
1	5640	263	1015	4.86	1068
2	5573	235	867	4.28	991
3	5146	203	715	3.42	873
4	2820	291	423	2.95	702
5	1366	518	110	2.62	495

the literature regarding the permittivity and Pockels coefficient of BTO between 200 MHz and several tens of GHz.

Furthermore, we demonstrated a comprehensive characterization of epitaxial thin-film BTO on a MgO substrate and determined characteristic domain sizes of  $\approx 1 \mu\text{m}$ .

Finally, we showed the potential of PLD-deposited BTO for electro-optic applications. Despite the presence of lattice mismatch-induced defects and initial in-plane growth followed by relaxation through defects, the BTO thin-film on the MgO substrate demonstrated excellent electro-optic properties. Our study emphasizes that also imperfect epitaxial thin-films can harness the potential of bulk BTO properties without a need of highest quality growths.

All of these findings suggest that BTO can offer remarkable performance even under non-ideal growth conditions, highlighting its versatility and potential for various applications in integrated photonics. It underscores the large potential of BTO for future electro-optic devices, potentially enabling the integration of tightly packed high-bandwidth PICs.

## 7. Experimental Section

**BTO Deposition:** Potential hydrogen absorption on the surface of a single-side polished MgO substrate (roughness  $R_a < 0.5 \text{ nm}$ ) was removed through ion milling.<sup>[30]</sup> The substrate then was loaded into the PLD where it is heated up to  $700 \text{ }^\circ\text{C}$  with an oxygen background of 200 mT. The laser fluence for the deposition was  $\approx 1.5 \text{ J cm}^{-2}$  with a repetition rate of 2 Hz. After deposition, the substrate was cooled down at  $5^\circ \text{ C min}^{-1}$  to room temperature in an oxygen background. The resulting film was 96 nm thick.

**Plasmonic Phase Shifter:** The BTO thin-film was structured with an inductively coupled plasma (ICP) etch with hydrogen silsesquioxane (HSQ) as protective mask. The remaining HSQ was removed with KOH. The amorphous Si layer was deposited with a plasma-enhanced chemical vapor deposition (PECVD) process and again etched with an ICP process, using a high-contrast e-beam polymer resists as a mask. The chip was annealed in an oxygen atmosphere to remove oxygen vacancies within the BTO layer. The 65 nm thick electrodes are deposited by thermal gold evaporation and subsequent lift-off.

**Debye Relaxation Fit Parameters:** The frequency ( $f$ ) dependence of the relative permittivity  $\epsilon_a(f)$  and Pockels  $r_{42}(f)$  data were fitted with two Debye relaxations, as suggested in<sup>[11c]</sup>

$$\left. \begin{aligned} \epsilon_a(f) \\ r_{42}(f) \end{aligned} \right\} = \frac{S_R \gamma_R^2}{\gamma_R^2 + f^2} + \frac{S_r \gamma_r^2}{\gamma_r^2 + f^2} + \epsilon_\infty \quad (3)$$

This accounts for the two relaxation mode's strengths ( $S_R, S_r$ ) and timescales ( $\gamma_R, \gamma_r$ ), as well as the high-frequency contributions  $\epsilon_\infty$ . In

the case of the Pockels constant  $r_{42}$ , parameters were found, as given in Table 1.

While for the relative permittivity  $\epsilon_a$ , parameters were obtained as given in Table 2.

## Acknowledgements

This work was supported in part by the EU Commission through the Horizon 2020 projects NEBULA (Grant 871658), plasmoniAC (Grant 871391), the EC Horizon Europe projects FLEX-SCALE 101096909, ALLEGRO 101092766, and the Swiss National Fund (SNF) project Nomad (200021\_208094). The authors gratefully thank the operations team of BRNC and ScopeM for their support and assistance put into this work. The authors further thank Prof. Wang for enabling the S11 VNA measurements. Electro-optic measurements had been recorded with the free and open-source tool "LabEXT".

## Conflict of Interest

The authors declare no conflict of interest.

## Data Availability Statement

The data that support the findings of this study are available from the corresponding author upon reasonable request.

## Keywords

BaTiO<sub>3</sub>, plasmonic devices, PLD, Pockels coefficient, relative permittivity

Received: August 9, 2023  
Revised: September 24, 2023  
Published online: October 17, 2023

- [1] P. J. Winzer, D. T. Neilson, *J. Lightwave Technol.* **2017**, *35*, 1099.
- [2] a) J. Lin, H. Sepehrian, L. A. Rusch, W. Shi, *Opt. Express* **2019**, *27*, 5610; b) R. A. Soref, J. P. Lorenzo, *Electron. Lett.* **1985**, *21*, 953; c) D. A. B. Miller, D. S. Chemla, T. C. Damen, A. C. Gossard, W. Wiegmann, T. H. Wood, C. A. Burrus, *Phys. Rev. Lett.* **1984**, *53*, 2173; d) S. A. Srinivasan, M. Pantouvaki, C. Porret, E. Vissers, P. Favia, J. De Coster, H. Bender, R. Loo, D. Van Thourhout, J. Van Campenhout, *IEEE J. Quantum Electron.* **2020**, *56*, 1.
- [3] E. L. Wooten, K. M. Kissa, A. Yi-Yan, E. J. Murphy, D. A. Lafaw, P. F. Hallemeier, D. Maack, D. V. Attanasio, D. J. Fritz, G. J. Mcbrien, D. E. Bossi, *IEEE J. Sel. Top. Quantum Electron.* **2000**, *6*, 69.
- [4] a) M. He, M. Xu, Y. Ren, J. Jian, Z. Ruan, Y. Xu, S. Gao, S. Sun, X. Wen, L. Zhou, L. Liu, C. Guo, H. Chen, S. Yu, L. Liu, X. Cai, *Nat. Photonics* **2019**, *13*, 359; b) P. Kharel, C. Reimer, K. Luke, L. He, M. Zhang, *Optica* **2021**, *8*, 357; c) P. O. Weigel, F. Valdez, J. Zhao, H. Li, S. Mookherjee, *J. Phys. Photonics* **2020**, *3*, 012001; d) A. Rahim, A. Hermans, B. Wohlfeil, D. Petousi, B. Kuyken, D. Van Thourhout, R. Baets, *Adv. Photon.* **2021**, *3*, 024003.
- [5] a) B. W. Wessels, *Annu. Rev. Mater. Res.* **2007**, *37*, 659; b) T. Naoyama, Y. Sakioka, M. Noda, M. Okuyama, K. Saito, *Jpn. J. Appl. Phys.* **2005**, *44*, 6873.
- [6] a) M. Zgonik, P. Bernasconi, M. Duelli, R. Schlessler, P. Günter, M. H. Garrett, D. Rytz, Y. Zhu, X. Wu, *Phys. Rev. B Condens. Matter.* **1994**, *50*, 5941; b) S. Kazaoui, J. Ravez, C. Elissalde, M. Maglione, *Ferroelectrics* **1992**, *135*, 85.

- [7] P. Bernasconi, M. Zgonik, P. Günter, *J. Appl. Phys.* **1995**, *78*, 2651.
- [8] D. Chelladurai, M. Kohli, Y. Horst, M. Eppenberger, L. Kulmer, T. Blatter, J. Winiger, D. Moor, A. Messner, C. Convertino, F. Eltes, Y. Fedoryshyn, J. Leuthold, presented at European Conf. on Optical Communication (ECOC) 2022, Optica Publishing Group, Washington DC, USA 2022.
- [9] J. Hlinka, T. Ostapchuk, D. Nuzhnyy, J. Petzelt, P. Kuzel, C. Kadlec, P. Vanek, I. Ponomareva, L. Bellaiche, *Phys. Rev. Lett.* **2008**, *101*, 167402.
- [10] J. L. T. Tsurumi, T. Hoshina, T. H. Kakemoto, *App. Phys. Lett.* **2007**, *91*, <https://doi.org/10.1063/1.2804570>.
- [11] a) A. V. Turik, N. B. Shevchenko, *Physica Status Solidi* **1979**, *95*, 5274; b) T. Hamano, D. J. Towner, B. W. Wessels, *Appl. Phys. Lett.* **2003**, *83*, 5274; c) K. Laabidi, M. D. Fontana, M. Maglione, B. Jannot, K. A. Müller, *Europhys. Lett.* **1994**, *26*, 309; d) M. Maglione, R. Böhmer, A. Loidl, U. T. Höchli, *Phys. Rev. B Condens. Matter* **1989**, *40*, 11441; e) M. P. Mcneal, S.-J. Jang, R. E. Newnham, *J. Appl. Phys.* **1998**, *83*, 3288; f) A. Von Hippel, *Rev. Mod. Phys.* **1950**, *22*, 221.
- [12] a) K. J. Kormondy, Y. Popoff, M. Sousa, F. Eltes, D. Caimi, M. D. Rossell, M. Fiebig, P. Hoffmann, C. Marchiori, M. Reinke, M. Trassin, A. A. Demkov, J. Fompeyrine, S. Abel, *Nanotechnology* **2017**, *28*, 075706; b) W. Guo, A. B. Posadas, A. A. Demkov, *J. Vac. Sci. Technol.* **2021**, *39*, 030804.
- [13] S. Vura, V. Jeyaselvan, R. Biswas, V. Raghunathan, S. K. Selvaraja, S. Raghavan, *ACS Appl. Electron. Mater.* **2021**, *3*, 687.
- [14] A. Messner, F. Eltes, P. Ma, S. Abel, B. Baeuerle, A. Josten, W. Heni, D. Caimi, J. Fompeyrine, J. Leuthold, *J. Lightwave Technol.* **2019**, *37*, 281.
- [15] X. Yang, X. Liu, S. Yu, L. Gan, J. Zhou, Y. Zeng, *Electronics* **2019**, *8*, 886.
- [16] M. D. Fontana, K. Laabidi, B. Jannot, M. Maglione, P. Jullien, *Solid State Commun.* **1994**, *92*, 827.
- [17] K. A. Müller, W. Berlinger, *Phys. Rev. B Condens. Matter* **1986**, *34*, 6130.
- [18] Yongqiang Shi, Lianshan Yan, A. E. Willner, *J. Lightwave Technol.* **2003**, *21*, 2358.
- [19] G. Völkel, K. A. Müller, *Phys. Rev. B* **2007**, *76*, 094105.
- [20] a) R. C. Miller, *Appl. Phys. Lett.* **1964**, *5*, 17; b) J. B. Khurgin, in *Non-linear Optics in Semiconductors II*, (Eds: R. K. Willardson, E. Garmire, A. Kost, E. R. Weber), Elsevier, Amsterdam, Netherlands **1998**.
- [21] J. F. Ihlefeld, D. T. Harris, R. Keech, J. L. Jones, J.-P. Maria, S. Trolier-Mckinstry, *J. Am. Ceram. Soc.* **2016**, *99*, 2537.
- [22] R. H. Buttner, E. N. Maslen, *Acta Crystallogr., Sect.: B Struct. Sci.* **1992**, *48*, 764.
- [23] B. D. Cullity, *Elements of X-ray Diffraction*, Addison-Wesley Publishing, Boston, USA **1956**.
- [24] A. S. Everhardt, S. Matzen, N. Domingo, G. Catalan, B. Noheda, *Adv. Electron. Mater.* **2016**, *2*, 1500214.
- [25] J. Kaneshiro, Y. Uesu, *Jpn. J. Appl. Phys.* **2011**, *50*, 09NE11.
- [26] G. Saerens, L. Lang, C. Renaut, F. Timpu, V. Vogler-Neuling, C. Durand, M. Tchernycheva, I. Shtrom, A. Bouravleuv, R. Grange, M. Timofeeva, *Opt. Express* **2019**, *27*, 19915.
- [27] M. Li, J. Zhou, X. Jing, M. Zeng, S. Wu, J. Gao, Z. Zhang, X. Gao, X. Lu, J. M. Liu, M. Alexe, *Adv. Electron. Mater.* **2015**, *1*, 1500069.
- [28] Y. A. Genenko, J. Glaum, M. J. Hoffmann, K. Albe, *Mater. Sci. Eng., B* **2015**, *192*, 52.
- [29] a) C. Dubourdieu, J. Bruley, T. M. Arruda, A. Posadas, J. Jordan-Sweet, M. M. Frank, E. Cartier, D. J. Frank, S. V. Kalinin, A. A. Demkov, V. Narayanan, *Nat. Nanotechnol.* **2013**, *8*, 748; b) A. B. Posadas, H. Park, M. Reynaud, W. Cao, J. D. Reynolds, W. Guo, V. Jeyaselvan, I. Beskin, G. Z. Mashanovich, J. H. Warner, A. A. Demkov, *ACS Appl. Mater. Interfaces* **2021**, *13*, 51230.
- [30] J. Geler-Kremer, A. B. Posadas, A. A. Demkov, *J. Vac. Sci. Technol.* **2020**, *38*, 062201.